Earth Dam on Liquefiable Foundation and Remediation: Numerical Simulation of Centrifuge Experiments

Zhaohui Yang, A.M.ASCE[1]; Ahmed Elgamal, M.ASCE[2]; Korhan Adalier, M.ASCE[3]; and Michael K. Sharp, M.ASCE[4]

Abstract: A series of four dynamic centrifuge model tests was performed to investigate the effect of foundation densification on the seismic performance of a zoned earth dam with a saturated sand foundation. In these experiments, thickness of the densified foundation layer was systematically increased, resulting in a comprehensive set of dam-foundation response data. Herein, Class-A and Class-B numerical simulations of these experiments are conducted using a two-phase (solid and fluid) fully coupled finite element code. This code incorporates a plasticity-based soil stress–strain model with the modeling parameters partially calibrated based on earlier studies. The physical and numerical models both indicate reduced deformations and increased crest accelerations with the increase in densified layer thickness. Overall, the differences between the computed and recorded dam displacements are under 50%. At most locations, the computed excess pore pressure and acceleration match the recorded counterparts reasonably well. Based on this study, directions for further improvement of the numerical model are suggested.

DOI: 10.1061/(ASCE)0733-9399(2004)130:10(1168)

CE Database subject headings: Dams, earth; Dam foundations; Liquefaction; Soil compaction; Numerical models; Earthquakes.

Introduction

Soil structures such as river dikes, highway embankments, and earth dams have been frequently damaged during past major earthquakes. This damage was often mainly due to liquefaction of the embankment and/or foundation soils (Seed 1968; 1970; Matsuo 1996; Krinitzsky and Hynes 2002). In most cases, large deformations occurred due to liquefaction of the supporting loose cohesionless foundation soil (Seed 1968; Tani 1996; Krinitzsky and Hynes 2002), resulting in cracking, settlement, lateral spreading, and slumping of the overlying soil structures.

Such earthquake liquefaction hazard necessitates the development of appropriate remediation countermeasures (Ledbetter et al. 1994; Marcuson et al. 1996). Recently, a series of highly instrumented centrifuge model tests was conducted at Rensselaer Polytechnic Institute (Adalier and Sharp 2002a,b), to experimentally assess the performance of countermeasure techniques for liquefiable earth dam foundations. In this experimental series, seismic behavior of a zoned earth dam with a saturated sand foundation (Fig. 1) was investigated under moderate levels of dynamic excitation. The effect of various parameters on the seismic behavior of the dam, such as the thickness, width, and depth of liquefiable layer, was studied (Adalier and Sharp 2002a). In all tests, the final permanent displacement field was carefully mapped. Such recorded deformation patterns provide insights towards the development of cost-effective remediation measures (Finn 2000; Adalier and Sharp 2002a).

The complementary data sets generated from this test series shed light on the underlying physical response mechanisms and deformation patterns, and offer an ideal opportunity for calibration and verification of numerical procedures. Herein, numerical predictions are performed for four tests, with different thickness of densified foundation layer. A two-phase (solid and fluid) fully coupled finite element (FE) program (Elgamal et al. 2002b; Yang and Elgamal 2002) is employed in the numerical analysis. This program incorporates a soil stress–strain model that has been calibrated earlier (Elgamal et al. 2002b) for Nevada No. 120 sand at a relative density D_r of about 40%. The same sand was used in this test series at two different D_r values (35 and 70%). Hence, the earlier calibration process served as a basis for defining modeling parameters in the current study. Initially, blind (Class-A) numerical predictions were conducted, only knowing the physical model configuration and the input motion. Based on comparison of the blind prediction results with the recorded data, an additional effort (Class-B simulation) was undertaken to adjust the soil modeling parameters.

In the following, after a brief description of the experimental and numerical modeling procedures, the blind prediction results are presented and compared to the corresponding experimental data. In addition, simulation results using the adjusted modeling parameters are briefly discussed. All computational and experimental results are reported below in prototype scale, unless otherwise specified.

[1]Assistant Project Scientist, Dept. of Structural Engineering, Univ. of California at San Diego, La Jolla, CA 92093.

[2]Professor, Dept. of Structural Engineering, Univ. of California at San Diego, La Jolla, CA 92093.

[3]Assistant Professor, Florida State Univ., Panama City, FL 32405.

[4]Director, Centrifuge Research Center, U.S. Army Engineer Research & Development Center, Vicksburg, MS 39180.

Note. Associate Editor: Roger G Ghanen. Discussion open until March 1, 2005. Separate discussions must be submitted for individual papers. To extend the closing date by one month, a written request must be filed with the ASCE Managing Editor. The manuscript for this paper was submitted for review and possible publication on May 6, 2003; approved on March 17, 2004. This paper is part of the ***Journal of Engineering Mechanics***, Vol. 130, No. 10, October 1, 2004. ©ASCE, ISSN 0733-9399/2004/10-1168–1176/$18.00.

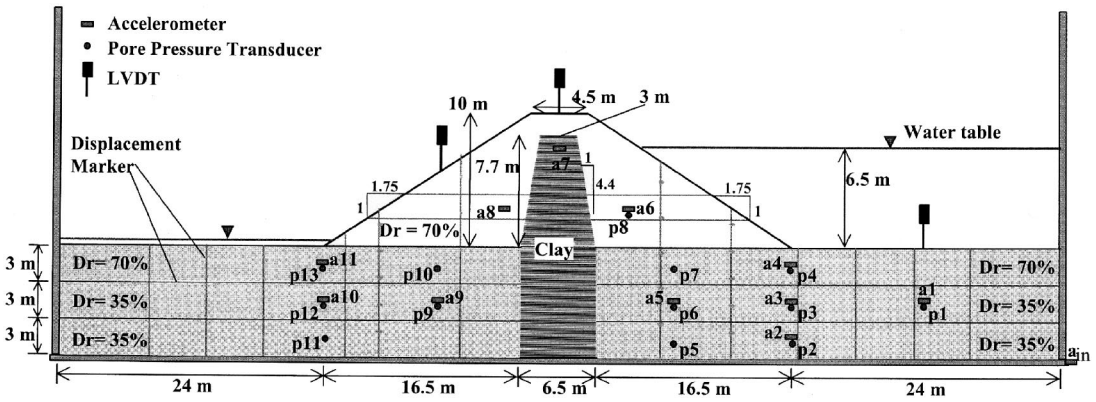

Fig. 1. Typical centrifuge model configuration (LLD case) and instrument deployment (Adalier and Sharp 2002a)

Centrifuge Testing Program

The liquefaction countermeasure experimental study (Adalier and Sharp 2002a, b) was conducted at a 100*g* gravitational acceleration. Under this gravity field, the centrifuge models (Fig. 1) simulated a prototype earth dam of 10 m in height and 39.5 m in width, resting on a sand foundation deposit of 9 m in thickness. The earth dam core was composed of Kaolin clay compacted at about 33% water content, with a dry unit weight of 13.4 kN/m^3 and an estimated unconfined shear strength (s_u) of 16–18 kPa. Clean Nevada No. 120 sand at a D_r of about 70% was used to construct the embankment slopes. The same sand was also used as the foundation material, at a D_r of about 35% (for the nondensified zone) and 70% (for the densified zone). The foundation layer was saturated with a fluid at a prototype permeability of about 1.3×10^{-4} m/s (D_r=35%) and 1.0×10^{-4} m/s (D_r=70%), within the range of fine sand (Lambe and Whitman 1969). Water was used as the reservoir fluid (Fig. 1), resulting in a prototype permeability of about 6×10^{-3} m/s within the embankment (in the range of coarse sand).

The four experiments (Fig. 1) were different only in thickness of the densified foundation layer, in order to evaluate overall performance of the dam–foundation system as a function of this parameter. The first case loose, loose, loose (LLL), was the benchmark test with the entire foundation composed of loose sand (35% D_r). The other three models loose, loose, dense (LLD), LDD, and DDD, represented an increasingly thicker densified foundation layer (70% D_r) of 3, 6, and 9 m, respectively (Fig. 1). Soil dynamic response was monitored (Fig. 1) by a large number of miniature accelerometers (in the lateral direction), pore pressure transducers, linear variable differential transformers (LVDTs), and a dense mesh of displacement markers.

All models were subjected to similar lateral excitation of about 30 cycles, 0.2*g* peak amplitude, and 1.5 Hz dominant frequency (Fig. 2). A free field site response analysis (using the FE numerical procedure to be discussed in the next section) showed that this base excitation would result in a peak ground acceleration (PGA) of 0.2*g* for the LLL and LLD foundation profiles, 0.25*g* for LDD, or 0.4*g* for DDD. The 0.4*g* PGA (on stiff ground) is an excitation level that would be hazardous to loose, saturated foundation soils as documented in case history studies (e.g., Krinitzsky and Hynes 2002). Finally, in all cases, the associated vertical excitation was less than 10% of the lateral input, and was not considered in the numerical simulations for simplicity.

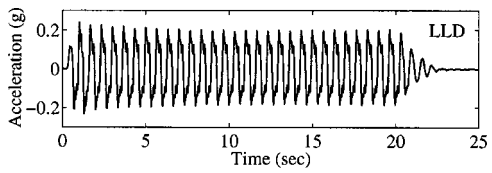

Fig. 2. Typical input base excitation (LLD case)

Numerical Modeling Procedures

Finite Element Model

To study the dynamic response of saturated soil systems as an initial-boundary-value problem, a two-dimensional plane–strain FE program was developed (Parra 1996; Yang and Elgamal 2002). The program implements the two-phase (solid–fluid) fully coupled FE formulation of Chan (1988) and Zienkiewicz et al. (1990). This implementation is based on the small-deformation theory, which does not account for nonlinearity effects due to finite deformation or rotation. In order to maintain focus on the conducted numerical study, the employed FE formulation is described in the Appendix.

A typical element employed in this formulation is shown in Fig. 3, with nine nodes for the solid phase and four nodes for the fluid phase, so as to reduce numerical difficulties associated with the nearly incompressible fluid phase (Chan 1988). Each solid node is associated with two-degrees-of-freedom (2 DOF) for the lateral and vertical displacement, and each fluid node is associated with 1 DOF for pore pressure. This 9-4-node element is employed in all numerical simulations presented herein.

The FE mesh for the dam-foundation system is shown in Fig. 3. Boundary conditions for all simulations were:

1. For the solid phase, lateral input motion was specified along the container boundary (base and two lateral sides), as the

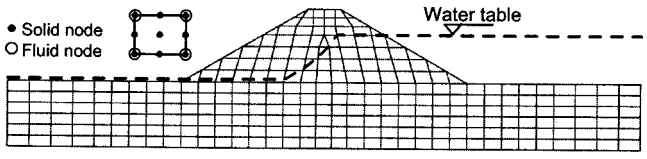

Fig. 3. Finite element mesh and employed solid–fluid coupled element

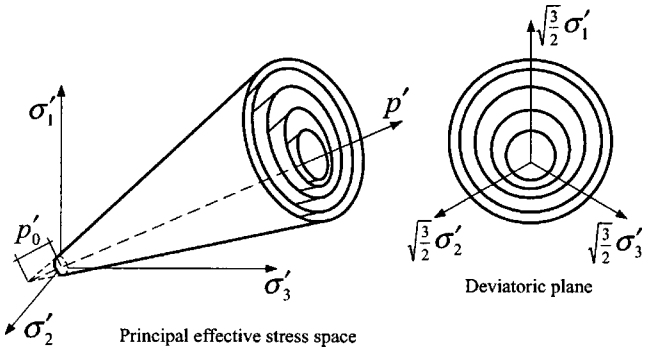

Fig. 4. Employed confinement–dependent yield surfaces for granular soils in principal stress space and deviatoric plane (after Prevost 1985; Parra 1996)

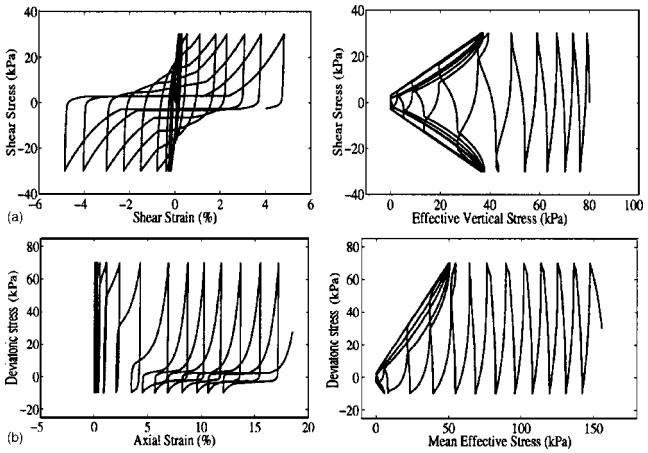

Fig. 5. Model simulation of stress-controlled, undrained cyclic shear loading: (a) without and (b) with static shear stress bias (Parra 1996; Elgamal et al. 2003)

recorded container acceleration (Fig. 2). All nodes on this boundary were fixed in the vertical direction.

2. For the fluid phase, the base and the two sides (i.e., the container boundaries) were impervious. The free water surface (phreatic surface) was assumed (for simplicity) to vary linearly within the clay core between the upstream side and the downstream side (dashed line in Fig. 3). At each node along the model surface, the acting hydrostatic pressure was specified.

A static application of gravity (model own weight) was performed before seismic excitation. The resulting fluid hydrostatic pressures and soil stress states served as initial conditions for the subsequent dynamic analysis.

Constitutive Model

The FE program incorporates a plasticity-based soil stress–strain constitutive model (Elgamal et al. 2003; Yang et al. 2003), in which a number of conical yield surfaces reproduce the nonlinear shear stress–strain response and the confinement dependence of shear strength (Fig. 4). A more detailed description of the model formulation is included in the Appendix. This soil model was calibrated earlier for the sand employed in the centrifuge tests, at a $D_r \approx 40\%$. The calibration phase (Elgamal et al. 2002b) included results of monotonic and cyclic laboratory sample tests (Arulmoli et al. 1992), as well as data from level-ground and mildly inclined infinite-slope dynamic centrifuge model tests (Dobry et al. 1995; Taboada 1995).

As mentioned in the Introduction, liquefaction-induced deformations are among the most important criteria for evaluation of related hazard. In this regard, the employed soil constitutive model was developed with emphasis on simulating the liquefaction-induced shear strain accumulation mechanism in clean medium-to-dense sands (Elgamal et al. 2002a,b, 2003, Yang and Elgamal 2002; Yang et al. 2003). Fig. 5(a) displays the characteristics of undrained model performance under symmetric stress-controlled cyclic shear loading conditions, in terms of shear stress-strain and effective stress path. The model response shows: (1) an initial phase of gradual loss in effective confinement and thus gradual increase in pore pressure (shear-induced contraction); (2) considerable shear strain accumulation within each load cycle, as the effective confinement approaches zero (i.e., liquefaction); and (3) increase in effective confinement at large cyclic shear strain excursions (shear-induced dilation), causing increased shear stiffness and strength. Fig. 5(b) depicts the characteristics of undrained triaxial response under anisotropically consolidated, cyclic loading conditions, showing the cycle-by-cycle accumulation of liquefaction-induced deformation.

Model Parameters

The main modeling parameters include typical dynamic soil properties such as low-strain shear modulus and friction angle, as well as calibration constants to control pore-pressure buildup rate, dilation tendency at large shear strains, and the level of liquefaction-induced shear deformation. Specific values of the major modeling parameters are listed in Table 1. For loose Nevada sand (35% D_r), the modeling parameters were essentially those identified from the earlier extensive calibration efforts for $D_r = 40\%$ (Elgamal et al. 2002b). For dense Nevada sand (70% D_r), no data were available for calibration, and the modeling parameters were chosen mainly based on extrapolating the $D_r = 40\%$ calibration results, available empirical formulae (Kramer 1996), and engineering judgment. Thus, the selected set of parameters produces higher shear strength and stiffness, stronger dilation tendency, and lower pore pressure buildup rate, compared to the $D_r = 40\%$ parameters.

For the clay core, a simplified (pressure-independent) version of the constitutive model was used, with a s_u of 17 kPa and zero friction angle. This shear strength was selected based on reported laboratory testing data (Adalier and Sharp 2002a).

Results and Discussion

Extensive discussion of the experimental results can be found in Adalier and Sharp (2002a,b). In this section, we first summarize the overall deformation pattern of the dam–foundation system (both experimental and computational), and compare the computed displacements at key locations to the experimental response. Thereafter, the computed acceleration and excess pore pressure are presented and compared to the corresponding experimental data at a number of representative spatial locations.

Deformation

Fig. 6 shows the measured and computed final deformed configurations, for the benchmark (LLL) and the lightly remediated

Table 1. Employed Major Modeling Parameters

Parameter	Nevada sand at D_r=35%	Nevada sand at D_r=70%	Kaolin clay	Nevada sand at D_r=70% (adjusted)
Low-strain shear modulus G_r (at 80 kPa mean effective confinement)	33.3 MPa	80.0 MPa	13.0 MPa	60.0 MPa
Friction angle ϕ	31.4°	35.5°	0.0°	35.5°
Cohesion	0.0 kPa	0.0 kPa	17.0 kPa	0.0 kPa
Liquefaction yield strain γ_y (Fig. 16, phase 1-2)	1.5%	0.0	0.0	0.0
Contraction parameter c_1 (Fig. 16, phase 0-1)	0.17	0.1	0.0	0.1
Contraction parameter c_2 (Fig. 16, phase 0-1)	0.05	0.05	0.0	0.05
Phase transformation angle ϕ_{PT}	26.5°	22.0°	0.0°	26.5°
Dilation parameter d_1 (Fig. 16, phase 2-3)	0.4	0.8	0.0	0.2
Dilation parameter d_2 (Fig. 16, phase 2-3)	10.0	10.0	0.0	10.0

(LLD) models. The overall deformation pattern of LLD is also representative of the LDD and DDD models (not shown here).

In all cases, due to combined action of the imparted lateral excitation and surcharge weight of the embankment, foundation soil migrated laterally towards the free field (lateral spreading). Lateral foundation displacement attained maximum values at ground surface, and decreased with depth. In the benchmark case [Fig. 6(a)], extensive liquefaction in the foundation resulted in: (1) large shear strains throughout the foundation layer and (2) severe distortion of the overlying dam body (with slope instability observed experimentally). In LLD [Fig. 6(b)], presence of the densified layer restrained the foundation from such excessive deformation. This in turn helped to maintain integrity of the overlying embankment.

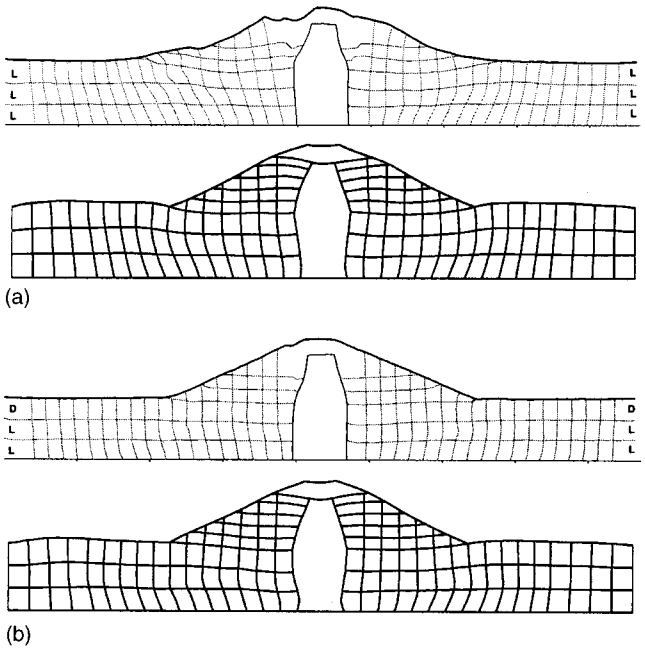

Fig. 6. Recorded and computed deformed configurations: (a) LLL and (b) LLD

In both physical models [Figs. 6(a and b)], the clay core experienced a nearly uniform lateral expansion along the foundation. This expansion (about 10% of the core width) was probably due to confinement reduction as the liquefied foundation sand migrated laterally towards the free field. Numerically, this nearly uniform core expansion was reproduced in the form of a barrel shape [Figs. 6(a and b)]. This barrel shape is a consequence of specifying all the bottom nodes to displace according to the input excitation, thus precluding the observed slippage between the clay core and container base.

Settlement

Fig. 7 depicts computed vertical displacement along with the corresponding LVDT data on the dam slopes and dam crest. In all cases, settlement is seen to accumulate on a cycle-by-cycle basis. Both the numerical and physical models indicate decreased settlement with the increase in densified layer thickness. However, the actual crest settlement was seen to accumulate at a gradually decreasing rate, in contrast to the linearly increasing settlement predicted by the numerical models. The experimentally observed decreasing settlement rate may be attributed to foundation densification and finite deformation effects that were not represented by the employed (small-strain) FE formulation. In the LLL

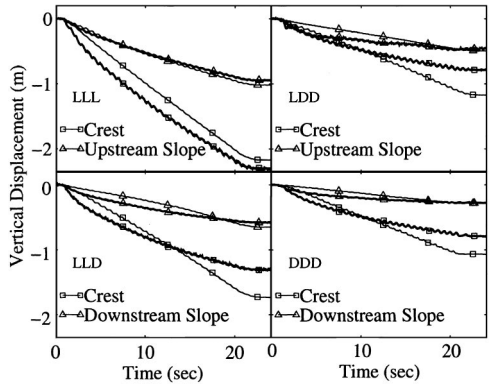

Fig. 7. Recorded linear variable differential, transformer (thicker) and computed (thinner) vertical settlements

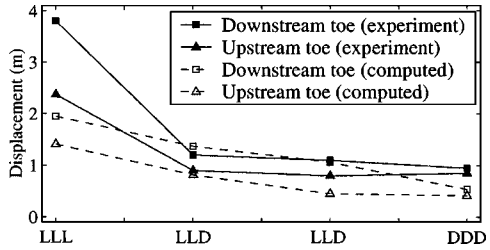

Fig. 8. Measured and computed lateral displacements at dam toes

case, computed and recorded crest settlements show a good agreement throughout the shaking event. In the other three cases, the numerical models initially under predicted but eventually over predicted the crest settlement. Finally, the predicted settlement history along the dam slopes was surprisingly good in all cases.

Lateral Deformation

The final lateral displacements at the dam toes are shown in Fig. 8 for all cases. In general, lateral movements are seen to decrease upon implementation of the foundation densification countermeasure. The final displacements were predicted reasonably well in the LLD and LDD cases, but were under predicted by 40–50% in the LLL and DDD cases. As mentioned above, a considerable portion of lateral displacement in the LLL case was due to embankment slope instability, which was not captured by the computational model. Better numerical results may be achieved by using a more refined FE mesh. On the other hand, the mismatch in DDD suggests the need for adjusting the extrapolated D_r = 70% sand properties (to allow for more deformation), as will be further discussed below (while comparing the acceleration and pore pressure responses).

It is of interest to observe that the experimental as well as the computational results show larger downstream lateral movements compared to the upstream side. This may be attributed to the presence of the laterally varying phreatic surface. The variable water table induced: (1) a fluid seepage force inside the clay core in the upstream–downstream direction (Li and Ming 2001) and (2) a higher initial (static) shear stress distribution on the downstream side of the models (Adalier and Sharp 2002a, b).

Stress–Strain Response

As mentioned above, the observed deformation patterns are mainly due to the cyclic-liquefaction mechanism (Fig. 5) developed in the saturated foundation soil. This is manifested in the computed shear stress–strain and effective stress path (Fig. 9) below the upstream dam toe, for the two extreme cases (i.e., LLL and DDD). In Fig. 9, the LLL stress path shows a major reduction in confinement during the first load cycle (due to pore pressure buildup). The corresponding shear stress–strain curve exhibits significant loss in shear stiffness and strength, with permanent shear strain accumulating at about 0.5% per cycle in the downslope direction. On the other hand, the much stronger DDD dilation tendency resulted in instantaneous regain in shear strength and effective confinement. The associated shear stress–strain curve shows asymmetric phases of rapid increase in shear stiffness and much less shear strain accumulation.

Remark: The models were subjected to a substantially long phase (30 cycles) of strong excitation (Fig. 2). In general, the numerically predicted displacements at key locations (dam toes and crest) compared reasonably well with the experimental counterparts, with the differences under 50% for all cases. It is clear that additional constitutive relation and numerical analysis refinement (e.g., finite-deformation formulation) need to be incorporated to more accurately capture the deformations associated with soil densification and geometric nonlinearity. Most notably however, the computational models were found to reproduce the predominant cycle-by-cycle lateral-spreading deformation mode of the dam-foundation system. This response mechanism dictated the pattern of acceleration and pore pressure response, as presented below.

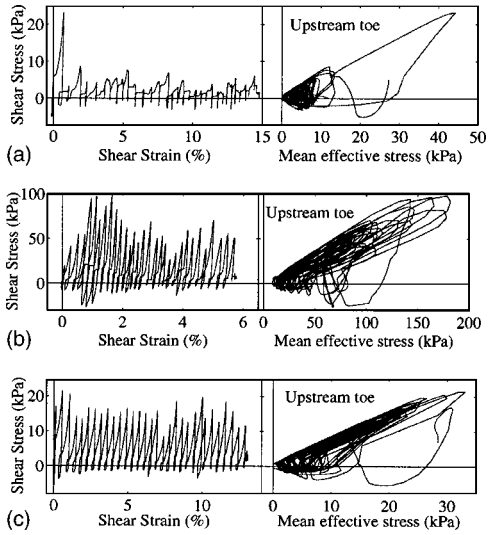

Fig. 9. Shear stress–strain and effective stress path at upstream under dam toe: (a) LLL case, (b) DDD case, and (c) DDD using modified dense sand parameters

Acceleration and Excess Pore Pressure

The acceleration and excess pore pressure responses are discussed with focus on three key locations: (1) downstream below the dam toe where lateral spreading displacement was most significant; (2) upstream below the dam body where significant lateral elongation occurred; and (3) below the dam crest, as an indicator of seismic energy imparted to the dam body.

Below Downstream Dam Toe

Fig. 10 depicts computed and recorded acceleration histories ($A10$) below the downstream dam toe. The asymmetric phases of dilative response discussed above (Fig. 9) instantaneously increased the soil shearing resistance, resulting in a pattern of strong asymmetric acceleration spikes as exhibited both computationally and experimentally in all cases. It may be seen that the computed acceleration response agrees well with the recorded data in all cases.

Fig. 11 depicts the computed and recorded excess pore pressure u_e histories at a nearby location ($P11$). In all cases (except DDD), the experimental results show a typical pattern of liquefaction response with excess pore pressure ratio r_u ($=u_e/\varsigma'_v$ where σ'_v is initial effective vertical stress) approaching 1.0 rapidly and remaining high thereafter. In general, the computed results show a close match with the recorded counterparts. However, in DDD where u_e was recorded in the dense sand layer, the computed results displayed much stronger instantaneous drops. This indicated that the extrapolated dense sand properties produced a stronger dilative response than that actually observed.

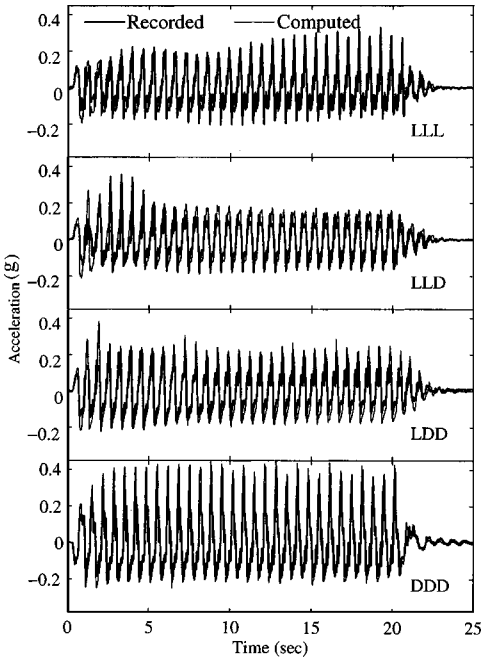

Fig. 10. Recorded and computed lateral acceleration histories downstream below dam toe (ACC 10)

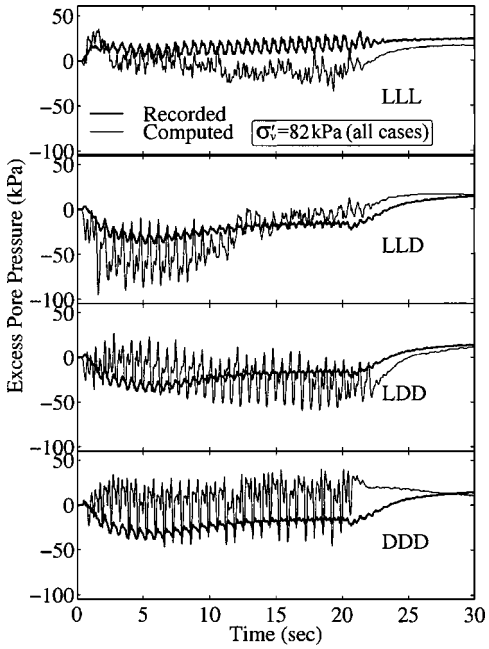

Fig. 12. Recorded and computed excess pore pressure histories at upstream below dam body (PPT 7)

It is worth noting that u_e response below the upstream dam toe (not shown) was similar to the downstream counterpart. On the upstream side, the acceleration response was also asymmetric but with negative spikes, denoting the accumulation of cyclic deformation opposite in direction to that of the downstream side (Elgamal et al. 2002a).

Below Upstream Dam Body

Directly below the dam body, spreading of the foundation soil (Fig. 6) led to low or even negative u_e buildup (*P*7), as depicted in Fig. 12. In particular, u_e response of the LLD and LDD cases showed: (1) gradual reduction in u_e during the shaking phase, as the soil expanded laterally and (2) significant u_e increase after the shaking (and deformation) stopped, as pore fluid redistributed into this area. This distinctive pattern of response was accurately reproduced by the numerical models. In cases where the response was monitored within the dense sand layer (all except LLL), the computed u_e again displayed stronger instantaneous drops (excessive dilation tendency). Finally, due to the low u_e at this location, the corresponding acceleration response displayed high amplitudes throughout (similar to Fig. 10).

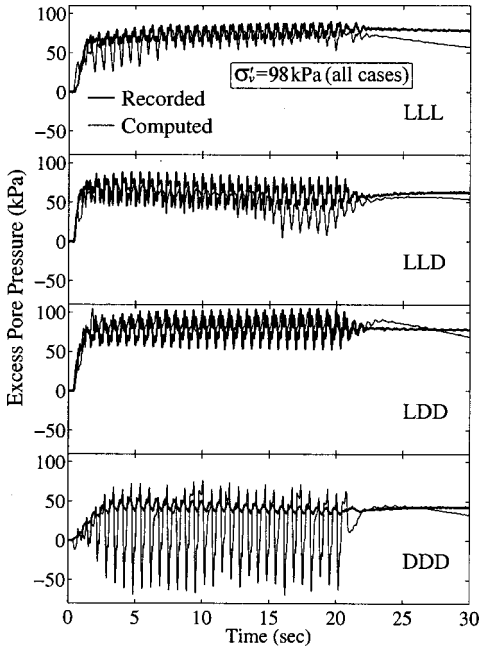

Fig. 11. Recorded and computed excess pore pressure histories downstream below dam toe (PPT 12)

Near Dam Crest

Fig. 13 depicts computed and recorded acceleration responses near the dam crest (*A*7), within the clay core. It is clearly seen that the acceleration amplitudes increased in proportion to the thickness of the densified foundation layer, as the denser foundation was able to transmit more seismic energy to the dam body (Adalier and Sharp 2002a).

In all cases, the numerical model somewhat over predicted the acceleration amplitudes. In addition, there is a phase difference between the recorded and the predicted acceleration response (most noticeable in DDD). These discrepancies are partially due to the much stronger dilation effects in the numerical model, as already indicated above. Furthermore, the hydrodynamic pressure induced by the upstream reservoir water, which was not considered in the numerical model, may have also contributed, although such hydrodynamic pressure is expected to be small for earth dams due to the mild slope inclination (e.g., Chopra 1967; Hall and Chopra 1982).

Remark: Due to the different initial stress states and material configurations, distinctive response patterns were observed at different locations of the dam-foundation system. Most of these response patterns were captured by the numerical models. Differences existed mainly in that the computed acceleration and u_e responses within the dense sand layer displayed larger spikes, indicating that the extrapolated dense sand dilation tendency

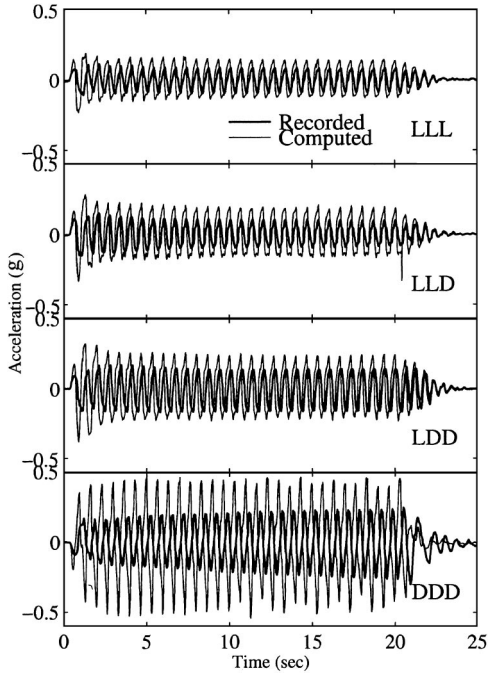

Fig. 13. Recorded and computed lateral acceleration histories at top of clay core (ACC 7)

should be reduced (Table 1). Additional simulations with adjusted dilatancy parameters resulted in improved comparisons in most response quantities, as discussed below.

Followup Class B Numerical Simulations

A set of adjusted model parameters for the densified sand (D_r =70%) is listed in Table 1. The low-strain shear modulus was decreased first (within the range reported in Kramer 1996). However, no appreciable effect was observed in these highly nonlinear liquefaction scenarios with immense reduction in effective confinement and shear stiffness. Thereafter, the phase transformation angle was increased, and the dilation parameter (d_1) was reduced. These adjustments resulted in much less dilation tendency, and more permanent shear strain accumulation [Fig. 9(c)].

Figs. 14 and 15 show, respectively, the computed u_e and acceleration responses at the locations discussed above (for LDD and DDD), using the adjusted dense sand parameters. Compared to the blind prediction results, significant overall improvement

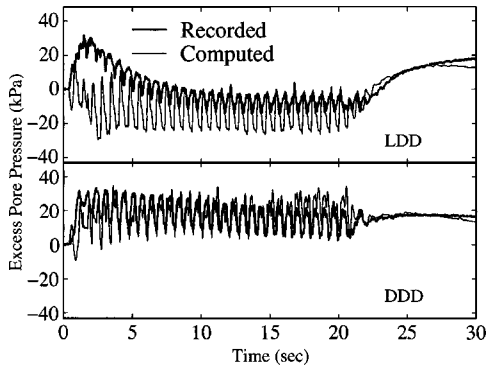

Fig. 14. Recorded and computed excess pore pressure histories at P7 (LDD and DDD) using adjusted dense sand parameters

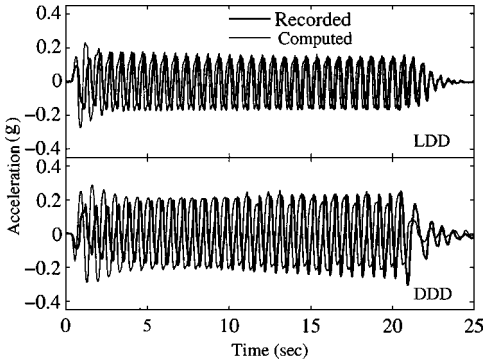

Fig. 15. Recorded and computed lateral acceleration histories at A7 (LDD and DDD) using adjusted dense sand parameters

may be observed. In particular, the strong u_e drops of the blind predictions (Fig. 12) were significantly reduced in the new simulations (Fig. 14). The computed acceleration response at *A*7, which was considerably over predicted before (Fig. 13), now shows a closer match, in both amplitude and phase (Fig. 15). The modified parameter set also resulted in as much as 0.2 m of additional lateral and vertical displacements, improving the results reported in Fig. 8.

Remarks

The centrifuge model test results yielded significant insights regarding the dynamic response characteristics of the embankment-foundation system and the effectiveness of various foundation densification schemes. Moreover, the comprehensive data sets generated are ideal for calibrating numerical models.

However, caution must be exercised when interpreting the test results, especially for the purposes of comparing these results to field data or for use in design. In particular, the presence of the rigid container in the centrifuge tests introduces artificial boundary effects that do not correspond to actual field conditions. Therefore, it is important to have a good assessment of the significance of these boundary effects on the model response. Indeed, additional numerical simulations (Yang et al. 2004) suggest that, using a flexible laminar container instead of a rigid one could result in lower amplitudes of embankment displacements and accelerations. The most reduction in response quantities were observed in the LLD and LDD cases, where the loose bottom layer serves effectively as a base isolator and prevents the lateral excitation from upward propagation. In these cases, the resulting displacements and accelerations were as little as 1/3 to 1/2 of the rigid container counterpart.

The employed base excitation (30 cycles of 0.2*g* harmonic motion, Fig. 2) has allowed for tracking the evolution of dam deformation under the same level of shaking intensity throughout. However, the consequences of such constant-amplitude shaking do not replicate those due to a seismic excitation record at the same PGA. Rather, seismic loading effects may be inferred indirectly using the numerical model after calibration. In summary, physical and numerical modeling techniques can be considered as a complement to available field observations and design procedures. Much research is needed to further advance these techniques, eventually leading to more reliable and economical dam design/remediation tools.

Summary and Conclusions

Using the same modeling parameters, a series of four blind numerical predictions were conducted to study the seismic behavior of an earth dam–foundation system, with different levels of foundation densification. Time histories of displacements, accelerations, and excess pore pressures computed at key locations were compared to the recorded counterparts. Computed displacements were close to those recorded on the slopes, and within 50% of the recorded crest settlement. The distinct observed acceleration and u_e response patterns at different regions of the dam-foundation system were reproduced reasonably well by the numerical models. Generally, the numerical models captured the predominant liquefaction response mechanism exhibited in the physical models, in terms of lateral spreading deformations and spiky acceleration response. Further adjustment of modeling parameters (mainly the dilation parameters of the dense sand) has improved the numerical simulation results to some extent. Additional constitutive relations and numerical techniques (e.g., finite deformation formulation) may be included for more accurate prediction of dam settlements and slope instability due to soil densification and geometric nonlinearity effects.

Acknowledgments

This work was supported by the Office of the Chief Engineers through the Earthquake Engineering Research Program of the U.S. Army Corps of Engineers, and by the Pacific Earthquake Engineering Research (PEER) Center, under the National Science Foundation Award No. EEC-9701568. The writers would like to thank the anonymous reviewers for their insightful comments.

Appendix. Description of the Computational Formulation

The saturated soil system is modeled as a two-phase material based on the Biot (1962) theory for porous media. A numerical formulation of this theory, known as $u-p$ formulation [in which displacement of the soil skeleton u, and pore pressure p, are the primary unknowns (Chan 1988, Zienkiewicz et al. 1990)], was implemented (Parra 1996; Yang 2000; Yang and Elgamal 2002).

The $u-p$ formulation may be defined in the following FE matrix form (Chan 1988):

$$\mathbf{M}\ddot{\mathbf{U}} + \int_{\Omega} \mathbf{B}^{\mathbf{T}}\boldsymbol{\sigma}' d\Omega + \mathbf{Q}\mathbf{p} - \mathbf{f}^{\mathbf{s}} = \mathbf{0} \tag{1a}$$

$$\mathbf{Q}^{\mathbf{T}}\dot{\mathbf{U}} + \mathbf{S}\dot{\mathbf{p}} + \mathbf{H}\mathbf{p} - \mathbf{f}^{\mathbf{p}} = \mathbf{0} \tag{1b}$$

where $\mathbf{M}$ = total total mass matrix; $\mathbf{U}$ = displacement vector; $\mathbf{B}$ = strain–displacement matrix; $\boldsymbol{\sigma}'$ = effective stress vector (determined by the soil constitutive model described below); $\mathbf{Q}$ = discrete gradient operator coupling the solid and fluid phases; $\mathbf{p}$ = pore pressure vector; $\mathbf{H}$ = permeability matrix; and $\mathbf{S}$ = compressibility matrix. The vectors $\mathbf{f}^{\mathbf{s}}$ and $\mathbf{f}^{\mathbf{p}}$ include the effects of body forces and prescribed boundary conditions for the solid–fluid mixture and the fluid phase, respectively.

Eq. (1) is integrated in time using a single-step predictor multicorrector scheme of the Newmark type (Chan 1988; Parra 1996). The solution is obtained for each time step using the modified Newton–Raphson approach (Parra 1996).

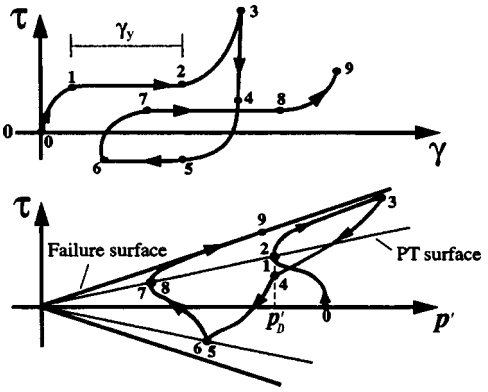

Fig. 16. Schematic of constitutive model response showing shear stress–shear strain and effective stress path under undrained shear loading conditions (Elgamal et al. 2003)

Soil Constitutive Model

The second term in Eq. (1*a*) is defined by the soil stress–strain constitutive model. The FE program incorporates a soil constitutive model (Parra 1996; Yang 2000; Elgamal et al. 2003; Yang et al. 2003) based on the original multisurface-plasticity (Fig. 4) theory for frictional cohesionless soils (Prevost 1985). It is recognized that soil shear strength is strongly dependent on the Lode angle. The employed conical yield surface (Fig. 4) may significantly overestimate soil strength along certain load paths. This discrepancy contributes to the overall uncertainty and approximations involved in the modeling effort reported herein.

The model was developed with emphasis on simulating the liquefaction-induced shear strain accumulation mechanism in clean medium-dense sands (Elgamal et al. 2002a,b, 2003, Yang and Elgamal 2002; Yang et al. 2003). Special attention was given to the deviatoric–volumetric strain coupling (dilatancy) under cyclic loading, which causes increased shear stiffness and strength at large cyclic shear strain excursions (i.e., cyclic mobility).

The flow rule is chosen so that the deviatoric component of flow is associative, and the volumetric component P'' defines the desired amount of dilation or contraction in accordance with experimental observations. Consequently, P'' defines the degree of non-associativity of the flow rule and is given by (Parra 1996)

$$P'' = \frac{(\eta/\overline{\eta})^2 - 1}{(\eta/\overline{\eta})^2 + 1}\Psi \tag{2}$$

where $\eta = ((3/2)\mathbf{s}:\mathbf{s})^{1/2}/p'$ = effective stress ratio; $\overline{\eta}$ = material parameter defining the stress ratio along the phase transformation (PT) surface (Ishihara et al. 1975); and Ψ = scalar function controlling the amount of dilation or contraction depending on the level of confinement and/or cumulated plastic deformation (Elgamal et al. 2003). The sign of $(\eta/\overline{\eta})^2 - 1$ dictates dilation or contraction. If negative, the stress point lies below the PT surface and contraction takes place (phase 0-1, Fig. 16). On the other hand, the stress point lies above the PT surface when the sign is positive and dilation occurs under shear loading (phase 2-3, Fig. 16). At low confinement levels, accumulation of plastic deformation may be prescribed (phase 1-2, Fig. 16) before the onset of dilation (Elgamal et al. 2003).

References

Adalier, K., and Sharp, M. K. (2002a). "Dynamic centrifuge modeling of earth dams on liquefiable ground." *Proc., 3rd U.S.–Japan Workshop on Advanced Research on Earthquake Engineering for Dams*, San Diego.

Adalier, K., and Sharp, M. K. (2002b). "Embankment dam on liquefiable foundation—Dynamic behavior and densification remediation." *J. Geotech. Eng.*, in press.

Arulmoli, K., Muraleetharan, K. K., Hossain, M. M., and Fruth, L. S. (1992). "VELACS: Verification of liquefaction analyses by centrifuge studies, laboratory testing program, soil data report." *Rep. Project No. 90-0562*, The Earth Technology Corporation, Irvine, Calif.

Biot, M. A. (1962). "The mechanics of deformation and acoustic propagation in porous media." *J. Appl. Phys.*, 33(4), 1482–1498.

Chan, A. H. C. (1988). "A unified finite element solution to static and dynamic problems in geomechanics." PhD dissertation, Univ. College of Swansea, Swansea, U.K.

Chopra, A. K. (1967). "Hydrodynamic pressures on dams during earthquakes." *J. Eng. Mech. Div.*, 93(6), 205–223.

Dobry, R., Taboada, V., and Liu, L. (1995). "Centrifuge modeling of liquefaction effects during earthquakes." *Keynote Lecture, Proc., 1st Intl. Conf. on Earthquake Geotechnical Engineering*, IS-Tokyo, K. Ishihara, ed., Vol. 3, Balkema, Rotterdam, The Netherlands, 1291–1324.

Elgamal, A., Parra, E., Yang, Z., and Adalier, K. (2002a). "Numerical analysis of embankment foundation liquefaction countermeasures." *J. Earthquake Eng.*, 6(4), 447–471.

Elgamal, A., Yang, Z., and Parra, E. (2002b). "Computational modeling of cyclic mobility and post-liquefaction site response." *Soil Dyn. Earthquake Eng.*, 22(4), 259–271.

Elgamal, A., Yang, Z., Parra, E., and Ragheb, A. (2003). "Modeling of cyclic mobility in saturated cohesionless soils." *Int. J. Plast.*, 19(6), 883–905.

Finn, W. D.L. (2000). "State-of-the-art of geotechnical earthquake engineering practice." *Soil Dyn. Earthquake Eng.*, 20, 1–15.

Hall, J. F., and Chopra, A. K. (1982). "Hydrodynamic effects in earthquake response of embankment dams." *J. Geotech. Eng. Div., Am. Soc. Civ. Eng.*, 108(4), 591–597.

Ishihara, K., Tatsuoka, F., and Yasuda, S. (1975). "Undrained deformation and liquefaction of sand under cyclic stresses." *Soils Found.*, 15(1), 29–44.

Kramer, S. L. (1996). *Geotechnical earthquake engineering*, Prentice Hall, Upper Saddle River, N.J.

Krinitzsky, E. L., and Hynes, M. E. (2002). "The Bhuj, India, earthquake: lessons learned for earthquake safety of dams on alluvium." *Eng. Geol. (Amsterdam)*, 66(3–4), 163–196.

Lambe, T. W., and Whitman, R. V. (1969). *Soil mechanics*, Wiley, New York.

Ledbetter, R. H., Liam Finn, W. D., Hynes, M. E., Nickell, J. S., Allen, M. G., and Stevens, M. G. (1994). "Seismic safety improvement of mormon island auxiliary dam," *2nd Seismic Short Course on Evaluation and Mitigation of Earthquake Induced Liquefaction Hazards*, Univ. of Southern California, Los Angeles.

Li, X. S., and Ming, H. Y. (2001). "Seepage effects on flow deformation of earth dam." *Proc., 2001 Mechanics and Materials Summer Conf.*, San Diego.

Marcuson, W. F., Hadala, P. F., and Ledbetter, R. H. (1996). "Seismic rehabilitation of earth dams." *J. Geotech. Eng.*, 122(1), 7–20.

Matsuo, O. (1996). "Damage to river dikes." *Soils Found.*, 36(1), 235–240.

Parra, E. (1996). "Numerical modeling of liquefaction and lateral ground deformation including cyclic mobility and dilation response in soil systems." PhD thesis, Rensselaer Polytechnic Institute, Troy, N.Y.

Prevost, J. H. (1985). "A simple plasticity theory for frictional cohesionless soils." *Soil Dyn. Earthquake Eng.*, 4(1), 9–17.

Seed, H. B. (1968). "Landslides during earthquakes due to soil liquefaction." *J. Geotech. Eng. Div., Am. Soc. Civ. Eng.*, 94(5), 1055–1123.

Seed, H. B. (1970). "Soil problems and soil behavior." *Earthquake engineering*, R. L. Wiegel, ed., Chap. 10, Prentice-Hall, Englewood Cliffs, N.J.

Taboada, V. M. (1995). "Centrifuge modeling of earthquake-induced lateral spreading in sand using a laminar box." PhD thesis, Rensselaer Polytechnic Institute, Troy, N.Y.

Tani, S. (1996). "Damage to earth dams." *Soils Found.*, 36(1), 263–272.

Yang, Z. (2000). "Numerical modeling of earthquake site response including dilation and liquefaction." PhD dissertation, Columbia Univ., New York.

Yang, Z., and Elgamal, A. (2002). "Influence of permeability on liquefaction-induced shear deformation." *J. Eng. Mech.*, 128(7), 720–792.

Yang, Z., Elgamal, A., Adalier, K., and Sharp, M. (2004). "Effect of container boundary on seismic embankment response in centrifuge model tests." *Proc., 11th Int. Conf. on soil Dynamics & Earthquake Engineering and 3rd Int. Conf. on Earthquake Geotechnical Engineering*, D. Doolin, A. Kammerer, T. Nogami, R. B. Seed, and I. Towhata, eds., Vol. 1, Univ. of California, Berkeley, Calif. 669–675.

Yang, Z., Elgamal, A., and Parra, E. (2003). "A computational model for cyclic mobility and associated shear deformation." *J. Geotech. Geoenviron. Eng.*, 129(12), 1119–1127.

Zienkiewicz, O. C., Chan, A. H.C., Pastor, M., Paul, D. K., and Shiomi, T. (1990). "Static and dynamic behavior of soils: a rational approach to quantitative solutions: I. fully saturated problems." *Proc. R. Soc. London, Ser. A*, 429, 285–309.